

On the estimation of ultimate tensile stress from small punch testing

Altstadt, E.; Houska, M.; Simonovski, I.; Bruchhausen, M.; Holmström, S.; Lacalle, R.;

Originally published:

February 2018

International Journal of Mechanical Sciences 136(2018), 85-93

DOI: <https://doi.org/10.1016/j.ijmecsci.2017.12.016>

Perma-Link to Publication Repository of HZDR:

<https://www.hzdr.de/publications/Publ-26303>

Release of the secondary publication
on the basis of the German Copyright Law § 38 Section 4.

CC BY-NC-ND

On the estimation of ultimate tensile stress from small punch testing

E. Altstadt ^{a,1}, M. Houska ^a, I. Simonovski ^b, M. Bruchhausen ^b, S. Holmström ^b, R. Lacalle ^c

^{a)} Helmholtz-Zentrum Dresden-Rossendorf (HZDR), Bautzner Landstrasse 400, 01328 Dresden (Germany)

^{b)} European Commission, Joint Research Centre (JRC), Westerduinweg 3, 1755 LE Petten, The Netherlands

^{c)} Universidad de Cantabria, INESCO Ingenieros, Avda. de los Castros, 39005 Santander (Spain)

¹⁾ Corresponding author, e-mail: e.altstadt@hzdr.de

Abstract

Finite element simulations of the small punch test are performed in order to critically evaluate and improve empirical correlations for the estimation of the ultimate tensile stress from force-deflection and force-displacement curves. For this purpose, generic elastic-plastic material properties are used. A systematic variation of the ultimate tensile stress and total uniform elongation is performed to investigate the effects of these parameters of the uniaxial stress-strain curve on the characteristics of small punch test curves. It is shown, that the maximum force F_m of the small punch test curve is not the appropriate parameter for the estimation of the ultimate tensile stress. Instead, the force F_i at a punch displacement of 1.29 times the specimen thickness (or alternatively at bottom deflection of 1.1 times the specimen thickness) should be used. This force is associated with the onset of plastic instability. A correlation between the force F_i and the ultimate tensile strength is proposed and validated by more than 100 small punch tests of nine different steel heats.

Keywords

small punch test; finite-element analysis; plasticity; hardening; ultimate tensile stress

Nomenclature

A_{gt}	total uniform elongation (percentage)
d	punch diameter
D	diameter of the receiving hole in the lower die
E	elastic modulus
F	punch force
F_i	punch force at onset of plastic instability
F_m	maximum punch force
h_0	initial thickness of the small punch specimen
n	material parameter
R_m	ultimate tensile stress
R_{p02}	yield stress (0.2% proof strength)
R^2	coefficient of determination
r_1	material parameter
T	temperature
u	central bottom deflection of the small punch specimen
u_i	central bottom deflection at onset of plastic instability
u_m	central bottom deflection at maximum force
v	punch displacement
v_i	punch displacement at onset of plastic instability
v_m	punch displacement at maximum force
α	material parameter
β_{Rm}	correlation factor for the estimation of R_m
$\bar{\varepsilon}$	nominal strain
ε	true strain
ε^{el}	true elastic strain
ε^{pl}	true plastic strain
$\bar{\sigma}$	nominal stress
σ	true stress
σ_{y0}	material parameter (initial flow stress)

1 Introduction

The small punch (SP) test has long been recognized as a supportive means for the development and monitoring of structural materials [1–6]. As a screening procedure, the SP test is intended to provide estimations of the material properties with as small amounts of material as possible, allowing for example a quick evaluation of ageing mechanisms such as radiation induced hardening and embrittlement or thermal ageing. The SP test has been used to estimate the ductile-to-brittle transition temperature [1,2,4], yield stress [7,8], ultimate tensile stress (UTS) [9,10], fracture toughness [11,12] and creep properties [13–17]. Detailed analyses of stress and strain in the SP disc have been performed by means of analytical elastic-plastic modelling [18,19] and by finite element calculations to underpin the empirical correlations [8,11,20]. A combination of finite element modelling, SP testing and neural networks was used to identify the parameters of the Gurson–Tvergaard–Needleman model for ductile damage [11] and of the Beremin model for brittle fracture [12]. A code of practice on SP testing was established in order to harmonize the various test set-ups and to achieve a better

comparability of the results of different labs [21]. An EN standard on SP testing of metallic materials is currently being developed under the auspices of ECISS TC 101 WG1. The following correlations have widely been used for the estimation of the ultimate tensile strength R_m [8,9,22–24]:

$$R_m = \beta_{Rm} \cdot F_m / h_0^2 \quad (1)$$

$$R_m = \beta_{Rm} \cdot F_m / (h_0 \cdot u_m) \quad (2)$$

with F_m being the maximum force and u_m the corresponding deflection (measured at the centre of the surface of the SP disc opposite to the punch), h_0 the initial specimen thickness and β_{Rm} an empirical coefficient. Instead of u_m the corresponding punch displacement v_m can be used in Eq. (2). An analysis of the differences between displacement v and deflection u can be found in [25]. A large number of comparative studies showed that Eq. (2) is more reliable as compared to Eq. (1), cf. e. g. [23,24,26,27]. Moreover, Kumar et al. [23] recently suggested that points of the force-deflection curve prior to (u_m, F_m) are even more suitable for the estimation of R_m .

In our paper, we follow this idea and present the results of finite element analyses with a systematic variation of the underlying plastic material properties. An improved correlation is proposed and validated with experimental data from nine different steels heats.

2 Finite element (FE) simulations

2.1 Details of the FE-models

The basic geometry of a SP set-up is shown in Figure 1. Two sets of geometrical parameters were used, G1 and G2 (cf. Table 1).

Table 1: Geometry parameters of the analysed SPT set-ups

Set No.	Punch diameter $d = 2r$ (mm)	Receiving hole diameter D (mm)	Specimen thickness h_0 (mm)	Edge size (mm)	Edge type
G1	2.5	4.0	0.5	0.2	Chamfer
G2	1.0	1.75	0.25	0.2	Chamfer

The finite element simulations were done with models including contact and friction. The commercial codes ANSYS® 14.5 (HZDR) and ABAQUS® (JRC) were used. In case of HZDR simulations, axisymmetric elements with 8 nodes, elastic-plastic material and large deformation and finite strain capability were used for the SP specimen. The element size was 50 µm. The lower die, the punch and the downholder were modelled by means of rigid lines interacting with the contact elements attached to the specimen surface. The friction coefficient for the contact areas between disc and punch was $\mu = 0.2$. The SP disc was fully clamped, i.e. relative motion between SP disc and lower die was prevented.

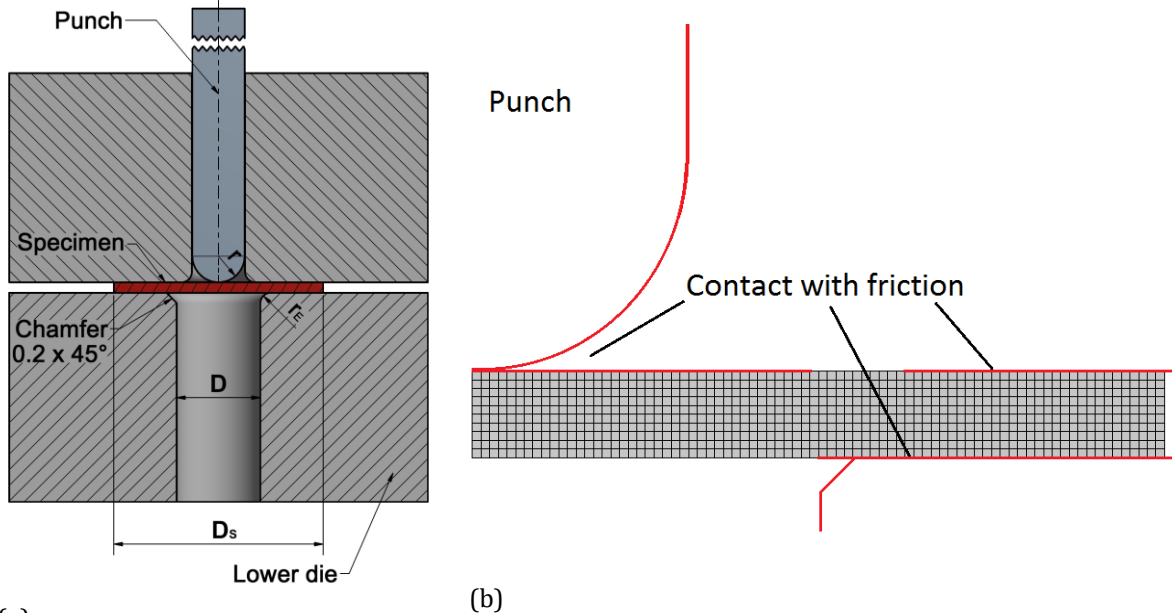


Figure 1: (a) Scheme of a SP test setup the edge of the receiving hole can either be a chamfer or a radius; (b) FE mesh (right).

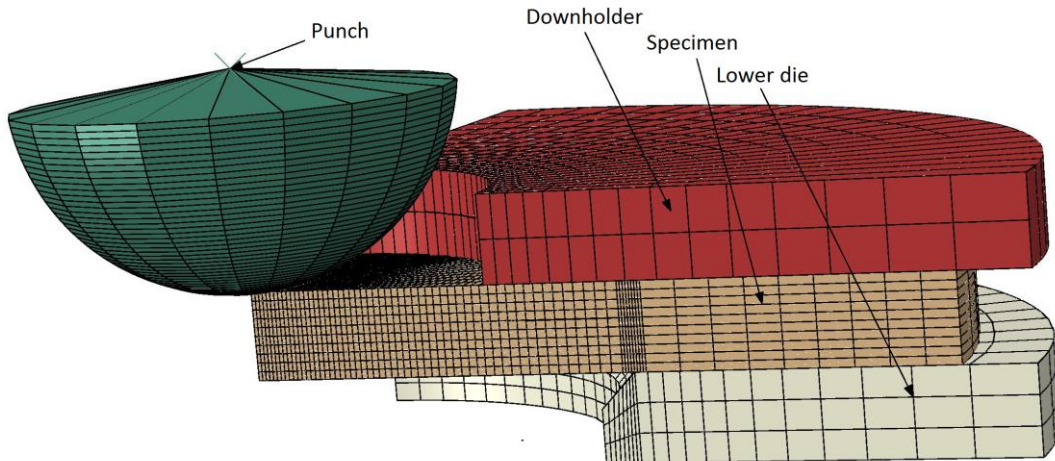


Figure 2: FE-mesh of JRC

JRC used a full 3D mesh with a quarter symmetry as shown in Figure 2. It was checked, that both the axisymmetric and the 3D mesh provided comparable results. The maximum difference of the simulated force-deflection curves was less than 5% for the maximum force F_m and less than 1% for the deflection at maximum force u_m . In section 2.2, the results for geometry set G1 are based on HZDR calculations and the results for set G2 are based on JRC calculations.

The plastic deformation was based on the following constitutive equation:

$$\sigma(\varepsilon^{pl}) = \sigma_{y0} + r_1 \cdot [\alpha \cdot \varepsilon^{pl} + 1 - \exp(-n\varepsilon^{pl})] \quad (3)$$

where σ is the true equivalent stress and ε^{pl} the true plastic equivalent strain. σ_{y0} , r_1 , α and n are material parameters. The parameter α represents the ratio of linear and exponential hardening. In this study $\alpha = 0$ was chosen. However, it was double-checked

that the conclusions of the simulations also hold for $\alpha > 0$. The corresponding uniaxial engineering (nominal) stress-strain curve $\bar{\sigma}(\bar{\varepsilon})$ is obtained by:

$$\begin{aligned}\bar{\varepsilon} &= \exp[\bar{\varepsilon}^{\text{pl}} + \bar{\varepsilon}^{\text{el}}] - 1 = \exp[\bar{\varepsilon}^{\text{pl}} + \sigma/E] - 1 \\ \bar{\sigma} &= \sigma / (1 + \bar{\varepsilon})\end{aligned}\quad (4)$$

with E being the elastic modulus. The overbar indicates engineering (nominal) values. In our simulation we used a generic material behaviour with a constant initial flow stress $\sigma_{y0} = 570$ MPa, constant elastic modulus $E = 212$ GPa, and a systematic variation of the hardening. In particular, the parameters r_1 and n were varied in such a way that specific values for the ultimate tensile stress, $R_m = \text{Max}[\bar{\sigma}(\bar{\varepsilon})]$, and the total uniform elongation, $A_{\text{gt}} = \bar{\varepsilon}|_{\bar{\sigma}=R_m}$, were obtained. The parameter variations are listed in Table 2.

There are four levels of ultimate tensile stress ($R_m = 650, 700, 800, 900$ MPa) and for each R_m four levels of total uniform elongation ($A_{\text{gt}} = 3\%, 6\%, 10\%, 20\%$). The stress-strain curves for $R_m = 900$ MPa are shown in Figure 3. In addition, the non-hardening case was analysed (ideal plasticity), i.e. $R_m = \sigma_{y0} = 570$ MPa. In this case, the true stress vs. true plastic strain curve is a horizontal line at 570 MPa.

Table 2: Material parameters

Code	r_1 (MPa)	n	R_{p02} (MPa)	R_m (MPa)	A_{gt} (%)
UTS_00	0	n. a.	n. a.	570	0.27
UTS_11	103.7	106.1	589	650	3
UTS_12	133.3	34.62	578	647	6
UTS_13	189.6	15.18	575	650	10
UTS_14	391.5	4.22	572	650	20
UTS_21	154.3	126.0	603	700	3
UTS_22	186.3	43.85	584	700	6
UTS_23	236.3	19.62	578	700	10
UTS_24	406.6	5.982	574	700	20
UTS_31	256.3	149.7	635	800	3
UTS_32	290.4	53.72	598	800	6
UTS_33	341.5	24.94	585	800	10
UTS_34	501.8	8.230	577	800	20
UTS_41	358.6	165.1	669	900	3
UTS_42	395.6	59.77	613	900	6
UTS_43	450.4	28.19	594	900	10
UTS_44	615.9	9.649	581	900	20

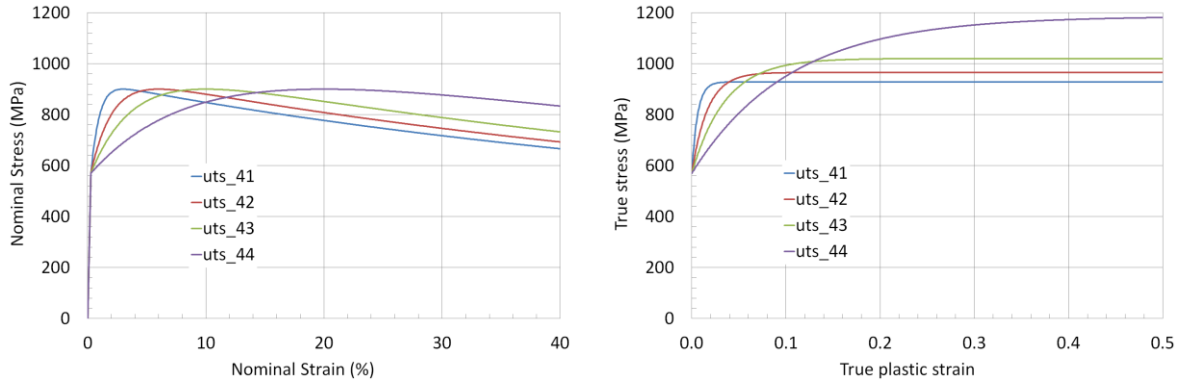


Figure 3: Generic stress-strain curves for $R_m=900$ MPa and varying A_{gt} (cases uts_4x); left: nominal stress vs. total nominal strain; right: true stress vs. true plastic strain

2.2 Simulation results

The force-deflection curves $F(u)$ and force-displacement curves $F(v)$ for the two geometry sets G1 and G2 are shown in Figure 4 and Figure 5. For each curve in a single diagram, the ultimate tensile stress R_m and σ_{y0} are the same, while the A_{gt} is varying ($A_{gt} = 3\%, 6\%, 10\%$ and 20%). It can be seen that the maximum forces F_m are significantly different, while the deflections at maximum force u_m are in a similar range. It can also be noticed that the curves in a single diagram exhibit a common pseudo intersection point. This intersection point, however, depends on the ultimate tensile stress R_m and also on the curve type (force-displacement or force-deflection). The locations of the intersection points u_i and v_i are summarized in Table 3.

Table 3: Parameters of intersection points

R_m (MPa)	Standard geometry (set G1)				Miniature geometry (set G2)			
	u_i (mm)	$F(u_i)$ (N)	v_i (mm)	$F(v_i)$ (N)	u_i (mm)	$F(u_i)$ (N)	v_i (mm)	$F(v_i)$ (N)
650	0.447	762	0.535	819	0.206	171	0.239	178
700	0.509	875	0.598	940	0.263	207	0.302	217
800	0.600	1107	0.686	1173	0.314	262	0.353	271
900	0.651	1318	0.759	1423	0.346	312	0.386	320
Average	0.552	--	0.645	--	0.282	--	0.320	--

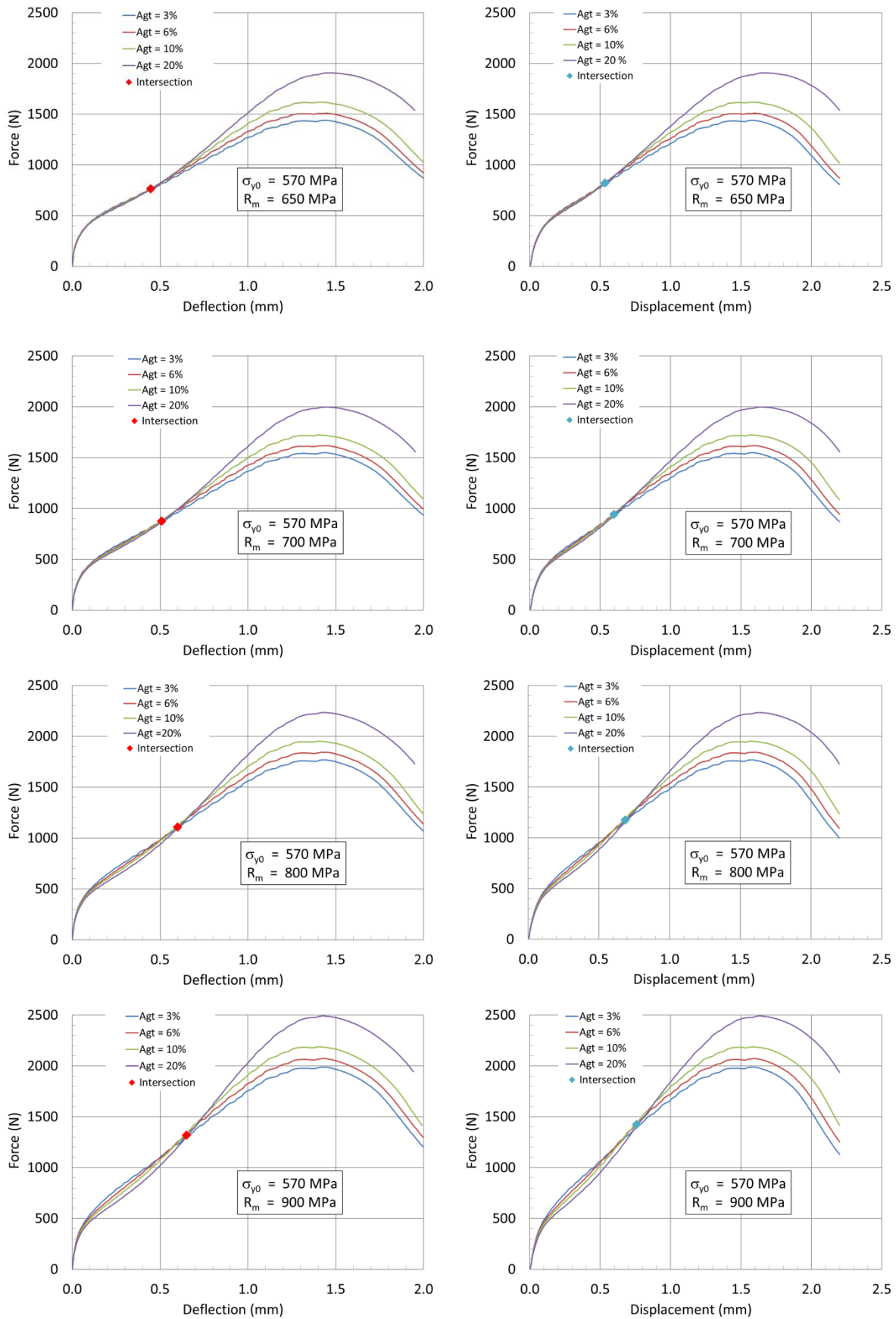


Figure 4: Force-deflection curves (left) and force-displacement curves (right) obtained from FE simulations, standard geometry (set G1)

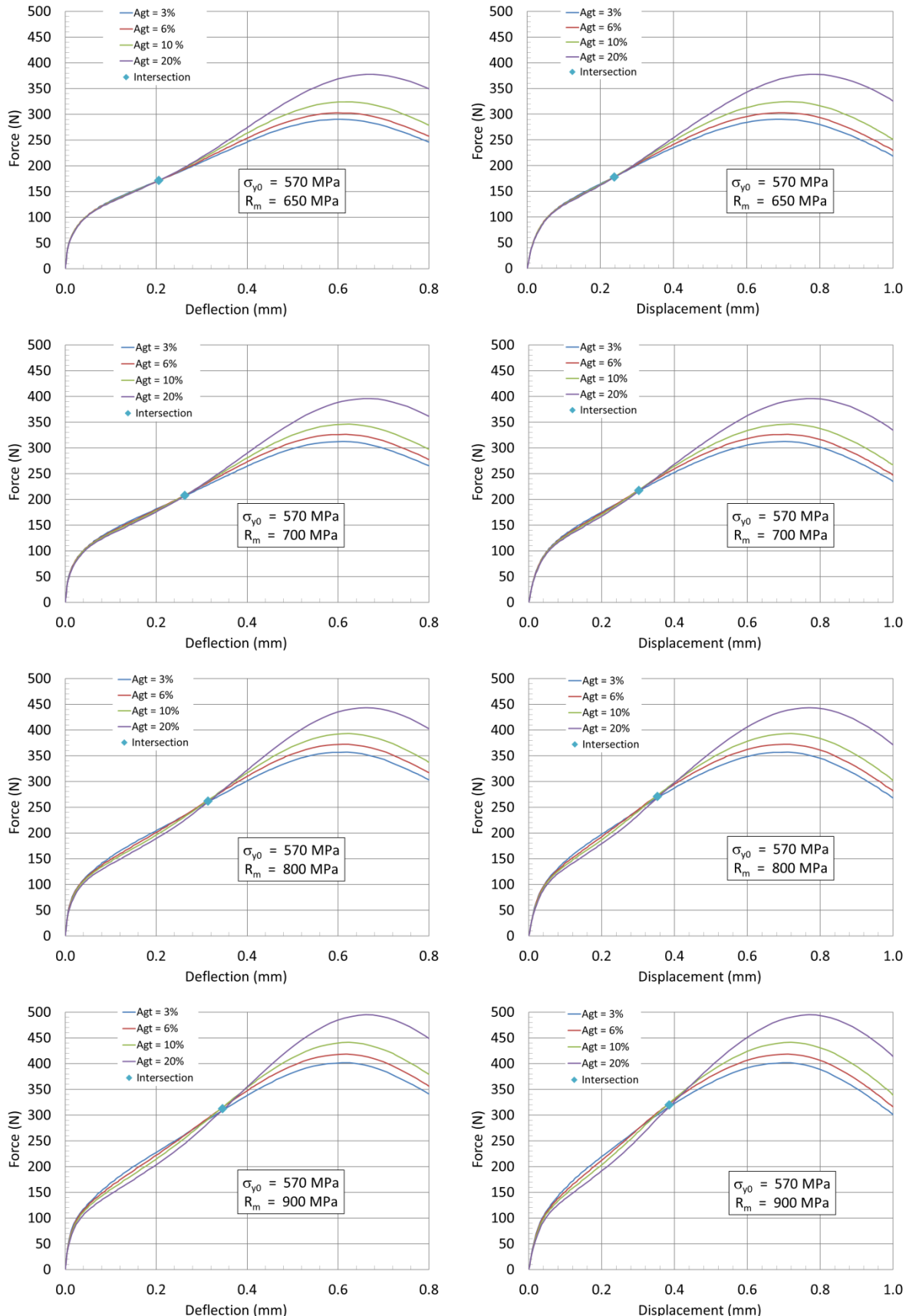


Figure 5: Force-deflection curves (left) and force-displacement curves (right) obtained from FE simulations, miniature geometry (set G2)

2.3 Simulation based correlations

In view of the results in section 2.2 it seems reasonable to use the force F_i instead of F_m for the correlation with the ultimate tensile stress in order to avoid a strong dependence of the correlation factor β_{Rm} on the tensile properties of the material. We propose the following equations to estimate the ultimate tensile stress:

$$\begin{aligned} R_m &= \beta_{Rm,u} \cdot F(\bar{u}_i) / h_0^2 \\ R_m &= \beta_{Rm,v} \cdot F(\bar{v}_i) / h_0^2 \end{aligned} \quad (5)$$

The average locations of the pseudo intersections in the SPT curves, \bar{u}_i and \bar{v}_i , shall be used to obtain the force F_i (cf. Table 3). For the sake of clarity it should be mentioned, that the division by h_0^2 is performed in order to get a dimensionless coefficient β_{Rm} . It does not mean that we would get the same β_{Rm} for specimen thicknesses other than $h_0 = 0.5$ mm or $h_0 = 0.25$ mm respectively; β_{Rm} is a function of all geometry parameters of the SPT set-up, including the specimen thickness. The correlation of the intersection force F_i with the ultimate tensile stress is shown in Figure 6. The resulting correlation factors and coefficients of determination are listed in Table 4.

Table 4: Coefficients for the estimation of ultimate tensile stress from numerical simulations according to Eq. (5)

Geometry	Curve type	$u_i v_i$	β_{Rm}	R^2
Standard (set G1)	$F(u)$	$u_i = 0.55$ mm	0.192	0.97
Standard (set G1)	$F(v)$	$v_i = 0.65$ mm	0.179	0.97
Miniature (set G2)	$F(u)$	$u_i = 0.28$ mm	0.205	0.96
Miniature (set G2)	$F(v)$	$v_i = 0.32$ mm	0.197	0.96

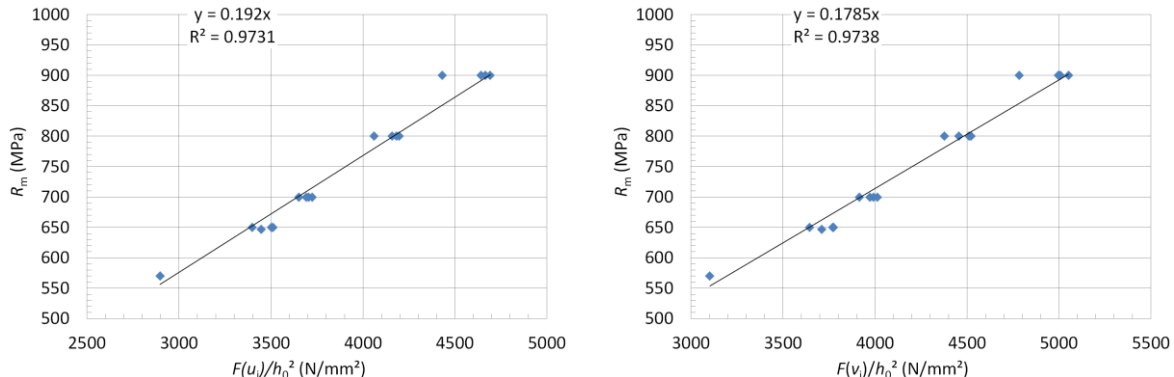


Figure 6: Correlation between intersection force F_i (from numerical simulations) and R_m , left: for bottom deflection, right: for punch displacement (set G1)

Now we analyse the thickness reduction in the specimen centre, $\Delta h = v - u$. It can be expected that the thickness reduction depends on the yield stress ratio $s = R_{p02}/R_m$ and the uniform strain $\bar{\epsilon}_{un}$. In Figure 7, the thickness reduction is shown in dependence on the punch displacement v for the cases UTS_4x and UTS_x3. It can be seen that $\Delta h(v)$ exhibits a steep slope in the beginning of the test which is due to the indentation of the punch into the SP specimen. After the initial increase the slope of $\Delta h(v)$ is small until the displacement reaches a value $v \approx 0.6$ mm. At this point the slope is significantly increasing again. The position of this point is approximately the same as v_i (cf. Table 4). This means, that at the intersection point (v_i, F_i) the onset of necking of the SP specimen occurs.

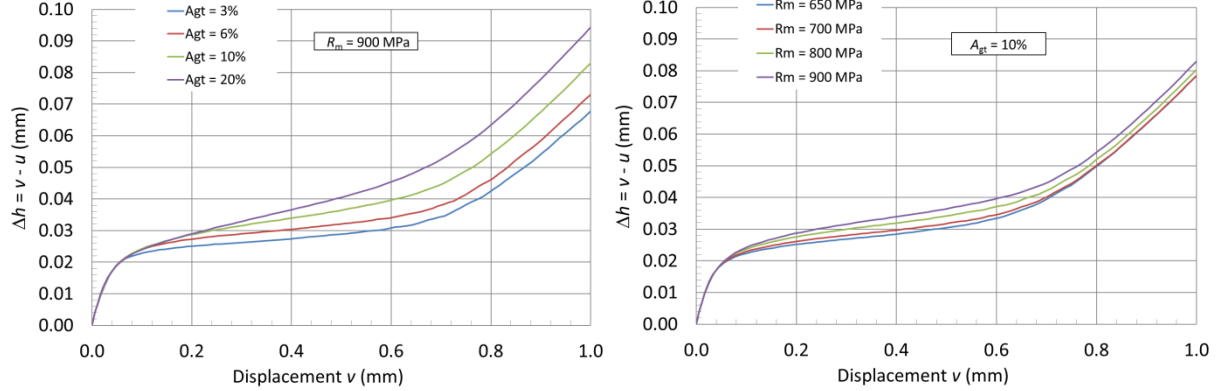


Figure 7: Central thickness reduction as a function of punch displacement for cases UTS_4x (left) and UTS_x3 (right), standard geometry (set G1)

3 Experimental validation

3.1 Materials

Three ferritic-martensitic (f/m) Cr-steels and two bainitic reactor pressure vessel steels were used for the experimental validation of the correlations Eqs. (2) and (5). Information on the materials and product forms are given in Table 5. The chemical compositions and the uniaxial tensile properties are listed in Table 6 and Table 7 respectively. The P92 was available in the as received condition and in four different heat treatments. In Table 7, the exponential fits are valid for the temperature range $-200^\circ\text{C} < T < 300^\circ\text{C}$, while the polynomial fits hold for $300^\circ\text{C} < T < 650^\circ\text{C}$.

Table 5: Materials overview

Material	Type	Product form	Heat treatment	Reference
P91	f/m steel	hot rolled pipe $\varnothing 360 \times 50$ mm	normalization $1040\text{-}1100^\circ\text{C} / 30$ min tempering $730\text{-}780^\circ\text{C} / 60$ min	[28]
P92	f/m steel	hot rolled pipe $\varnothing 219 \times 22$ mm	AR: standard normalization + tempering HT1: AR + $800^\circ\text{C} / 2$ h HT2: AR + $760^\circ\text{C} / 2$ h HT3: AR + $750^\circ\text{C} / 2$ h HT4: AR + $740^\circ\text{C} / 2$ h	[29]
Eurofer97	f/m steel	hot rolled plate 14.5 mm	normalization $980^\circ\text{C}/27$ min/air cooling tempering $760^\circ\text{C}/90$ min/air cooling	[30,31]
22 NiMoCr 3 7	bainitic steel reactor pressure vessel Biblis C		890°C/4h/water quenching 650°C/7h/air cooling	[32]
15Kh2MFA	bainitic steel reactor pressure vessel Greifswald unit 8		original RPV manufacturing technology	[33]

Table 6: Chemical compositions in wt%

Material	C	Si	V	Cr	Mn	Ni	Mo	Al	P	S	Cu	Nb	W
P91	0.116	0.464	0.23	9.50	0.507	0.09	0.91	0.0195	0.0085	0.0006	n.a.	0.09	n.a.
P92	0.12	0.24	0.19	8.56	0.53	0.13	0.43	0.009	0.012	0.009	0.050	0.062	1.63
Eurofer97	0.11	0.04	0.2	8.82	0.47	0.02	n.a.	n.a.	0.005	n.a.	0.0016	n.a.	1.09
22 NiMoCr 3 7	0.215	0.20	0.007	0.42	0.91	0.88	0.53	0.018	0.008	0.007	0.04	n.a.	n.a.
15Kh2MFA	0.15	0.30	0.31	2.86	0.45	0.10	0.79	n.a.	0.008	0.009	0.05	n.a.	0.01

Table 7: Tensile properties at room temperature and temperature fit of R_{p02} and R_m

Material	$R_{p0.2}$ (MPa)	R_m (MPa)	A_{gt} (%)	A_t (%)	$R_{p0.2}(T)$ ⁽¹⁾ (MPa)	$R_m(T)$ ⁽¹⁾ (MPa)
P91	538	686	9.4	19.9	$466+658*\exp(-0.0072*T)$	$557+675*\exp(-0.0054*T)$
P92-AR	679	808	6.1	18.0	polynomial ⁽²⁾	polynomial ⁽³⁾
P92-HT1	502	675	11.4	26.8	n.a.	n.a.
P92-HT2	541	707	9.6	24.4	n.a.	n.a.
P92-HT3	574	726	7.8	21.4	n.a.	n.a.
P92-HT4	584	733	7.7	21.6	n.a.	n.a.
Eurofer97	544	662	6.6	25.1	$456+644*\exp(-0.0067*T)$	$413+485*\exp(-0.0022*T)$
22 NiMoCr 3 7	424	591	10.9	23.9	$349+571*\exp(-0.0069*T)$	$515+572*\exp(-0.0068*T)$
15Kh2MFA	532	649	7.2	20.3	$512+2026*\exp(-0.0159*T)$	$553+770*\exp(-0.0071*T)$

⁽¹⁾ T in K⁽²⁾ $-118 + 2.92*T - 2.91*10^{-3}*T^2 + 1.56*10^{-7}*T^3$ (valid for 573 K \leq T \leq 923 K)⁽³⁾ $678 + 0.269*T + 2.69*10^{-4}*T^2 - 1.06*10^{-6}*T^3$ (valid for 573 K \leq T \leq 923 K)

3.2 Small punch tests

A number of 115 small punch tests were performed at HZDR with the standard geometry (Table 1, set G1). The test data for P92 is stored in an online database [29]. Additional sixteen high temperature SP tests on the P92-AR steel were performed at JRC. The specimens were cut to a thickness of 0.6 mm by means of an electrical discharge machine and subsequently ground with grit 2500 to final thickness. The individual final thickness of each specimen was measured. The maximum accepted thickness tolerance was $\pm 5 \mu\text{m}$. All tests were performed at a displacement rate of 0.5 mm/min. The displacement v was measured by an inductive sensor with an accuracy of $\pm 1 \mu\text{m}$. A correction for the compliance of the punch was applied ($C_p = 4.98 \cdot 10^{-5} \text{ mm/N}$).

Table 8: Overview of small punch tests

Material	Number of tests	Test temperatures (°C)
P91	23	-177 ... +331
P92-AR	3 + 16	room temperature, 300 ... 650
P92-HT1	5	room temperature
P92-HT2	4	room temperature
P92-HT3	3	room temperature
P92-HT4	5	room temperature
Eurofer97	8	-24 ... +250
22 NiMoCr 3 7	31	-151 ... +332
15Kh2MFA	33	-150 ... +332

The force-displacement curves $F(v)$ of SP tests at room temperature are shown in Figure 8 (one curve per material as listed in Table 8). The $F(v)$ curves of the material P91 for different temperatures are shown in Figure 9. The curve for $T = -173^\circ\text{C}$ represents a brittle failure, the other test curves represent ductile failure. By using 9 different materials and heats, and by testing selected materials at different temperatures, a wide variation of tensile properties is obtained.

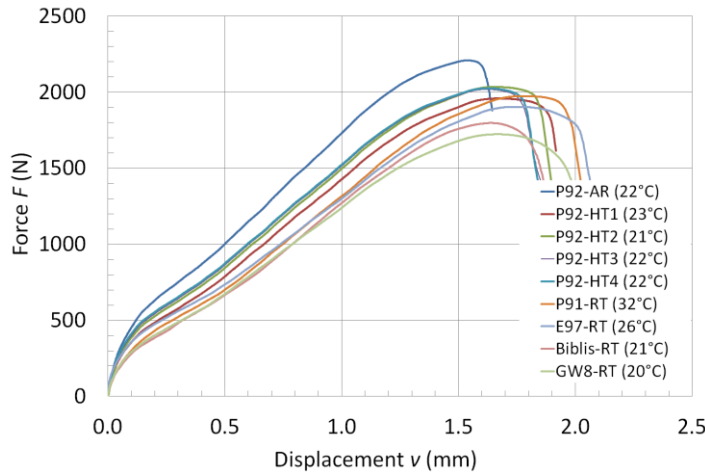


Figure 8: Force-displacement curves from SP tests at room temperature for the materials listed in Table 8

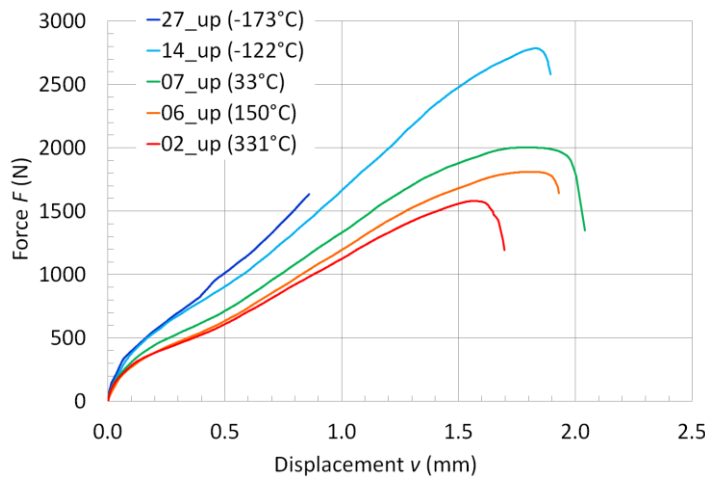


Figure 9: Force-displacement curves from SP tests at different temperatures for the material P91

3.3 Results and correlations

The evaluation of the SP tests is based on the force-displacement curves $F(v)$. The characteristic parameters v_m , F_m and F_i were determined for all tests. This is illustrated for a test of material 15Kh2MFA in Figure 10. In accordance with the given geometry and the curve type, the location of F_i is $v_i = 0.65$ mm (cf. Table 1 and Table 4).

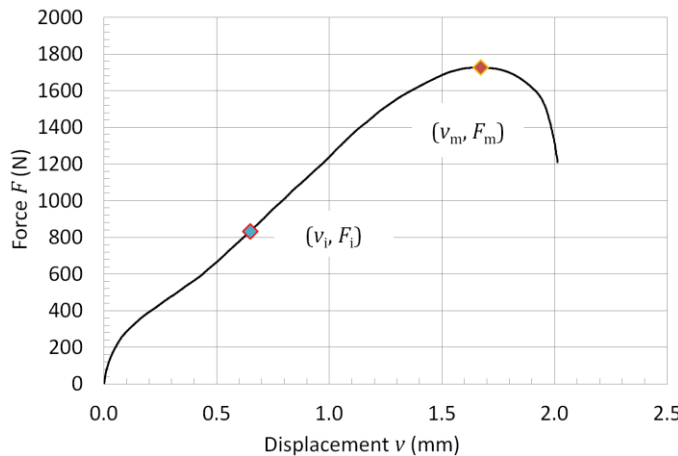


Figure 10: Force-displacement curve of the material 15Kh2MFA tested at room temperature (test no. 06) with indication of the characteristic parameters
 $F_i = 831$ N (at $v_i = 0.65$ mm)
 $v_m = 1.67$ mm
 $F_m = 1727$ N

Based on this analysis, we correlate the ultimate tensile stress from the uniaxial tensile tests R_m (cf. Table 7) with $F_m/(h_0 * v_m)$ and F_i/h_0^2 from the SP tests. This provides

experimental values for the correlation factor β_{Rm} . The coefficient of determination R^2 gives a quantitative measure of the goodness of the SP based estimation of the ultimate tensile stress. Moreover, in case of the F_i based correlation Eq. (5), the experimental correlation factor β_{Rm} can be compared with the one obtained from the FE simulations (cf. section 4). The correlations are shown in Figure 11 and Figure 12. The slopes of the regression lines (with forced intercept at zero) correspond to the coefficient β_{Rm} in Eq. (2) and Eq. (5) respectively. This regression analysis includes all SP tests (all materials). We also analysed these correlations per material. The results are listed in Table 9.

Table 9: Slopes β_{Rm} and coefficients of determination R^2 per material

Material	R_m versus $F_m/(h_0 \cdot v_m)$		R_m versus F_i/h_0^2	
	β_{Rm}	R^2	β_{Rm}	R^2
P91	0.277	0.706	0.193	0.958
P92 (AR, HT1-HT4)	0.287	0.951	0.171	0.964
Eurofer97	0.299	0.555	0.181	0.728
22 NiMoCr 3 7	0.254	0.528	0.175	0.875
15Kh2MFA	0.291	0.661	0.193	0.913
All materials	0.278	0.747	0.183	0.870

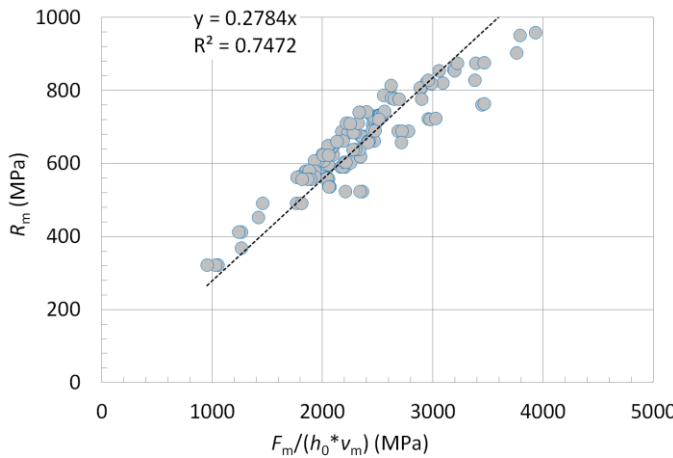


Figure 11: Correlation between R_m from uniaxial tensile tests and $F_m/(h_0 \cdot v_m)$ from the SP tests according to Eq. (2)

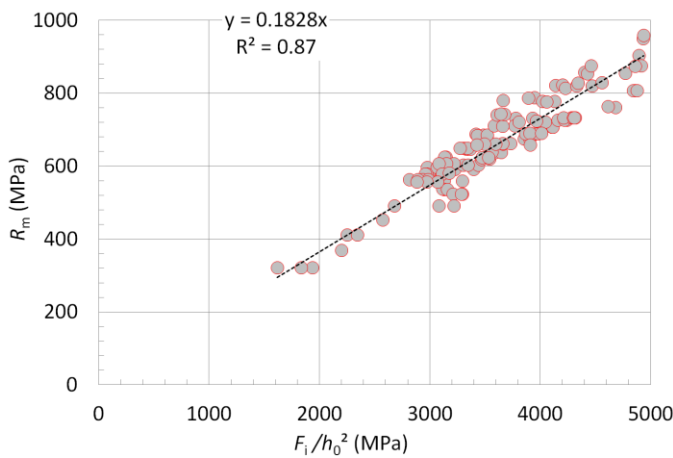


Figure 12: Correlation between R_m from uniaxial tensile tests and F_i/h_0^2 from the SP tests according to Eq. (5)

Figure 13 shows an example of the central thickness reduction $\Delta h(u)$ for P92-AR obtained from simultaneous measurements of displacement v and deflection u . The displacement value of $v_i = 0.65$ mm proposed in the correlation Eq. (5) is also included in the figure. It can be seen, that this value is close to the onset of plastic instability (rapid increase of the slope the curve) which is the phenomenon linked to R_m in uniaxial tensile tests.

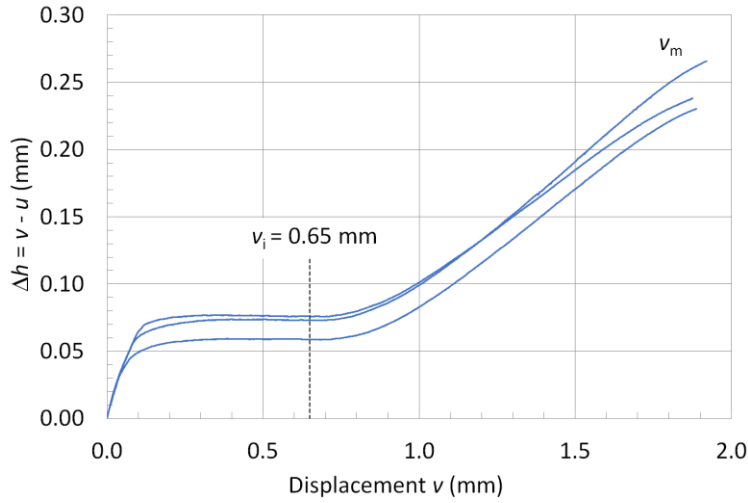


Figure 13: Central thickness reduction, Δh , as a function of punch displacement, v , for the P92-AR steel

4 Discussion

As shown in section 2.2, the maximum forces F_m strongly depend on the hardening behaviour of the material. For generic materials with identical ultimate tensile stress R_m , the F_m values significantly increase with increasing uniform strain, while the deflections at maximum force u_m are in a similar range. This is due to the fact that the plastic strain in the SP specimen at maximum force is by far larger than the uniform strain in a tensile test [11,23,27]. This means that neither Eq. (1) nor Eq. (2) are appropriate for the estimation of R_m . This is additionally substantiated by the work of Foulds et al. [34]. They found that the “crack initiates well in advance of the peak load, undergoing stable growth up to the peak load”. In contrast, the force F_i can be associated with the onset of plastic instability and is therefore better suited for a correlation with the ultimate tensile stress R_m of the uniaxial tensile test. The correlations between R_m and $F_m/(h_0*v_m)$ on one hand and between R_m and F_i/h_0^2 on the other hand, which are based on experiments on five different steels (nine heats), confirm the findings of the FEM simulation with generic material properties. We put emphasis on the fact that the F_i based correlation coefficient β_{Rm} obtained from the experiments (0.183) agrees very well with the one obtained from the simulations (0.179) even though the tensile properties of the real materials (section 3.1) and those of the generic materials (section 2.1) are different. This underpins the assumption that the correlation Eq. (5) is only weakly dependent on the tensile properties of the investigated material. Finally, the F_i based correlation Eq. (5) is also valid for brittle failure in the SP test since the specimen fails at a displacement $v > v_i$ (cf. Figure 9, test at -173 °C). In contrast, the F_m based correlation Eq. (2) leads to a systematic overestimation of R_m as it can be seen from Figure 11 where the three rightmost data points originate from SP tests with brittle failure.

5 Conclusions

Correlations based on the maximum force F_m of the small punch test and the uniaxial ultimate tensile stress cannot be independent of the material properties.

In contrast, correlations based on the small punch force F_i are only weakly dependent on the tensile properties and should therefore be preferred for the estimation of the ultimate tensile stress.

The location of the characteristic force F_i depends on the geometry of the small punch test set-up and on the curve type (force-deflection or force-displacement).

6 References

- [1] J. Kameda, A kinetic model for ductile-brittle fracture mode transition behavior, *Acta Metall.* 34 (1986) 2391–2398. doi:10.1016/0001-6160(86)90142-2.
- [2] T. Misawa, T. Adachi, M. Saito, Y. Hamaguchi, Small punch tests for evaluating ductile-brittle transition behavior of irradiated ferritic steels, *J. Nucl. Mater.* 150 (1987) 194–202. doi:10.1016/0022-3115(87)90075-4.
- [3] G.E. Lucas, Review of small specimen test techniques for irradiation testing, *Metall. Trans. A.* 21 (1990) 1105–1119. doi:10.1007/BF02698242.
- [4] J. McNaney, G.E. Lucas, G.R. Odette, Application of ball punch tests to evaluating fracture mode transition in ferritic steels, *J. Nucl. Mater.* 179–181 (1991) 429–433. doi:10.1016/0022-3115(91)90116-0.
- [5] J.S. Ha, E. Fleury, Small Punch Tests on Steels for Steam Power Plant (I), *KSME Int. J.* 12 (1998) 818–826.
- [6] X. Jia, Y. Dai, Small punch tests on martensitic/ferritic steels F82H, T91 and Optimax-A irradiated in SINQ Target-3, *J. Nucl. Mater.* 323 (2003) 360–367. doi:10.1016/j.jnucmat.2003.08.018.
- [7] J. Kameda, X. Mao, Small-punch and TEM-disc testing techniques and their application to characterization of radiation damage, *J. Mater. Sci.* 27 (1992) 983–989. doi:10.1007/BF01197651.
- [8] E.N. Campitelli, P. Spätiq, R. Bonadé, W. Hoffelner, M. Victoria, Assessment of the constitutive properties from small ball punch test: experiment and modeling, *J. Nucl. Mater.* 335 (2004) 366–378. doi:10.1016/j.jnucmat.2004.07.052.
- [9] X. Mao, H. Takahashi, Development of a further-miniaturized specimen of 3 mm diameter for tem disk (\varnothing 3 mm) small punch tests, *J. Nucl. Mater.* 150 (1987) 42–52. doi:10.1016/0022-3115(87)90092-4.
- [10] R. Hurst, K. Matocha, Where are we now with the European Code of Practice for Small Punch Testing?, in: Proc. 2nd Int. Conf. SSTM „Determination Mech. Prop. Mater. Small Punch Miniat. Test. Tech., Ostrava, Czech Rep., 2012: pp. 4–18.
- [11] M. Abendroth, M. Kuna, Identification of ductile damage and fracture parameters from the small punch test using neural networks, *Eng. Fract. Mech.* 73 (2006) 710–725. doi:10.1016/j.engfracmech.2005.10.007.
- [12] T. Linse, M. Kuna, J. Schuhknecht, H.-W. Viehrig, Usage of the small-punch-test for the characterisation of reactor vessel steels in the brittle–ductile transition region, *Eng. Fract. Mech.* 75 (2008) 3520–3533. doi:10.1016/j.engfracmech.2007.03.047.
- [13] M.L. Saucedo-Muñoz, S.-I. Komazaki, T. Takahashi, T. Hashida, T. Shoji, Creep property measurement of service-exposed SUS 316 austenitic stainless steel by the small-punch creep-testing technique, *J. Mater. Res.* 17 (2002) 1945–1953. doi:10.1557/JMR.2002.0288.
- [14] P. Dymáček, K. Milička, Creep small-punch testing and its numerical simulations, *Mater. Sci. Eng. A.* 510–511 (2009) 444–449. doi:10.1016/j.msea.2008.06.053.
- [15] G. Chen, P.C. Zhai, Q.J. Zhang, Creep Properties of SUS304 Steel by Small Punch Creep Tests, *Mater. Sci. Forum.* 631–632 (2009) 387–392. doi:10.4028/www.scientific.net/MSF.631-632.387.
- [16] D. Blagoeva, Y.Z. Li, R.C. Hurst, Qualification of P91 welds through Small Punch creep testing, *J. Nucl. Mater.* 409 (2011) 124–130. doi:10.1016/j.jnucmat.2010.09.015.

- [17] B. Gülcimen, P. Hähner, Determination of creep properties of a P91 weldment by small punch testing and a new evaluation approach, *Mater. Sci. Eng. A*. 588 (2013) 125–131. doi:10.1016/j.msea.2013.09.029.
- [18] J. Chakrabarty, A theory of stretch forming over hemispherical punch heads, *Int. J. Mech. Sci.* 12 (1970) 315–325. doi:10.1016/0020-7403(70)90085-8.
- [19] T.S. Byun, E.H. Lee, J.D. Hunn, K. Farrell, L.K. Mansur, Characterization of plastic deformation in a disk bend test, *J. Nucl. Mater.* 294 (2001) 256–266. doi:10.1016/S0022-3115(01)00484-6.
- [20] I. Simonovski, S. Holmström, M. Bruchhausen, Small punch tensile testing of curved specimens: Finite element analysis and experiment, *Int. J. Mech. Sci.* 120 (2017) 204–213. doi:10.1016/j.ijmecsci.2016.11.029.
- [21] European Committee for Standardization (CEN), CWA 15627: Small Punch Test Method for Metallic Materials, (2007).
- [22] P. Dymáček, F. Dobeš, P. Král, J. Dvořák, INVESTIGATION OF FRACTURE IN PURE ALUMINIUM AFTER ECAP BY MEANS OF SMALL PUNCH TEST, *Acta Metall. Slovaca - Conf.* 3 (2013). doi:10.12776/amsc.v3i0.107.
- [23] K. Kumar, A. Pooleery, K. Madhusoodanan, R.N. Singh, J.K. Chakravartty, R.S. Shriwastaw, B.K. Dutta, R.K. Sinha, Evaluation of ultimate tensile strength using Miniature Disk Bend Test, *J. Nucl. Mater.* 461 (2015) 100–111. doi:10.1016/j.jnucmat.2015.02.029.
- [24] M. Bruchhausen, S. Holmström, I. Simonovski, T. Austin, J.-M. Lapetite, S. Ripplinger, F. de Haan, Recent developments in small punch testing: Tensile properties and DBTT, *Theor. Appl. Fract. Mech.* 86 (2016) 2–10. doi:10.1016/j.tafmec.2016.09.012.
- [25] M.F. Moreno, G. Bertolino, A. Yawny, The significance of specimen displacement definition on the mechanical properties derived from Small Punch Test, *Mater. Des.* 95 (2016) 623–631. doi:10.1016/j.matdes.2016.01.148.
- [26] T.E. García, C. Rodríguez, F.J. Belzunce, C. Suárez, Estimation of the mechanical properties of metallic materials by means of the small punch test, *J. Alloys Compd.* 582 (2014) 708–717. doi:10.1016/j.jallcom.2013.08.009.
- [27] E. Altstadt, H.E. Ge, V. Kuksenko, M. Serrano, M. Houska, M. Lasan, M. Bruchhausen, J.-M. Lapetite, Y. Dai, Critical evaluation of the small punch test as a screening procedure for mechanical properties, *J. Nucl. Mater.* 472 (2016) 186–195. doi:10.1016/j.jnucmat.2015.07.029.
- [28] S. Kohlar, Gefüge und Eigenschaften des warmfesten Chromstahls P91, Helmholtz-Zentrum Dresden-Rossendorf, Dresden, 2009. <http://nbn-resolving.de/urn:nbn:de:bsz:d120-qucosa-229778>.
- [29] M. Houska, E. Altstadt, SP tests on P92 (T70175) at RT, version 1.0, European Commission JRC, [Catalog], (2017). <http://dx.doi.org/10.5290/24>.
- [30] C. Heintze, C. Recknagel, F. Bergner, M. Hernández-Mayoral, A. Kolitsch, Ion-irradiation-induced damage of steels characterized by means of nanoindentation, *Nucl. Instrum. Methods Phys. Res. Sect. B Beam Interact. Mater. At.* 267 (2009) 1505–1508. doi:10.1016/j.nimb.2009.01.122.
- [31] A.A.F. Tavassoli, A. Alamo, L. Bedel, L. Forest, J.M. Gentzbittel, J.W. Rensman, E. Diegele, R. Lindau, M. Schirra, R. Schmitt, H.C. Schneider, C. Petersen, A.M. Lancha, P. Fernandez, G. Filacchioni, M.F. Maday, K. Mergia, N. Boukos, N. Baluc, P. Spätić, E. Alves, E. Lucon, Materials design data for reduced activation martensitic steel type EUROFER, *J. Nucl. Mater.* 329–333 (2004) 257–262. doi:10.1016/j.jnucmat.2004.04.020.

- [32] C. Zurbuchen, Influence of Specimen Type, Crack Length and Evaluation Method on Quasi-Static and Dynamic Fracture Toughness Properties, in: Proceedings of the ASME 2009 Pressure Vessels and Piping Conference, Prague, 2009: pp. 511–517. doi:10.1115/PVP2009-77796.
- [33] H.-W. Viehrig, M. Scibetta, K. Wallin, Application of advanced master curve approaches on WWER-440 reactor pressure vessel steels, *Int. J. Press. Vessels Pip.* 83 (2006) 584–592. doi:10.1016/j.ijpvp.2006.04.005.
- [34] J. Foulds, P. Woytowitz, T. Parnell, C. Jewett, Fracture Toughness by Small Punch Testing, *J. Test. Eval.* 23 (1995) 3. doi:10.1520/JTE10392J.